draft version February 20, 2012
Preprint typeset using LaTeX style emulateapj v. 11/26/04

arXiv:1202.3852v1 [astro-ph.CO] 17 Feb 2012

THE SL2S GALAXY-SCALE GRAVITATIONAL LENS SAMPLE. I: THE ALIGNMENT OF MASS AND LIGHT IN MASSIVE EARLY-TYPE GALAXIES AT $Z = 0.2 - 0.9$

Raphaël Gavazzi[1], Tommaso Treu[2†], Philip J. Marshall[3,4,2], Florence Brault[1], and Andrea Ruff[5]

draft version February 20, 2012

ABSTRACT

We study the relative alignment of mass and light in a sample of 16 massive early-type galaxies at $z = 0.2 - 0.9$ that act as strong gravitational lenses. The sample was identified from deep multiband images obtained as part of the Canada France Hawaii Legacy Survey (CFHTLS) as part of the Strong Lensing Legacy Survey (SL2S). Higher resolution follow-up imaging is available for a subset of 10 systems. We construct gravitational lens models and infer total enclosed mass, elongation, and position angle of the mass distribution. By comparison with the observed distribution of light we infer that there is a substantial amount of external shear $\langle\gamma_{\rm ext}\rangle \approx 0.12$, arising most likely from the environment of the SL2S lenses. In a companion paper (Ruff et al. 2011) we combine these measurements with follow-up Keck spectroscopy to study the evolution of the stellar and dark matter content of early-type galaxies as a function of cosmic time.

Subject headings: galaxies: fundamental parameters — gravitational lensing —

1. INTRODUCTION

The last two decades have seen the emergence of a standard model of galaxy formation. The main ingredients, dominating the overall dynamics of the universe, are non-relativistic particles that do not interact with light or baryons except through gravity (i.e. cold dark matter), and the mysterious dark energy (Perlmutter et al. 1999; Riess et al. 1998), i.e. a term in the stress-energy tensor of the universe characterized by negative pressure (or equivalently a cosmological constant).

The familiar standard model particles move and interact with each other within this skeleton of unkown particles and fields (White & Rees 1978). Although standard model particles represent only a small minority of the total energy budget of the universe (Komatsu et al. 2011), they play a crucial role in the formation of galaxies, and their constituents stars and planets. In those overdense regions of the universe, interactions between standard model particles alter their dynamics and spatial distribution. Indirectly, through gravitational interactions, this so-called "baryonic physics" in turn modifies the properties of the underlying dark matter distribution (Blumenthal et al. 1986; Gnedin et al. 2004; Duffy et al. 2010). Understanding the interplay between baryons and dark matter at sub-galactic scales is crucial not only for any effort to understand how galaxies form and evolve, but also may shed light on the properties of the dark matter itself (e.g., self-interaction cross-section Spergel & Steinhardt 2000; Loeb & Weiner 2011).

From an observational point of view, it is very challenging to measure accurately the relative distribution of baryonic and dark matter on sub-galactic scales. By-and-large, traditional methods require the presence of a luminous tracer (e.g. hot plasma, cold gas, or stars), whose kinematics are then interpreted to reconstruct the underlying gravitational potential (e.g. Saglia et al. 1992; Gerhard et al. 2001; Humphrey et al. 2006; Franx et al. 1994). Those methods have been used to demonstrate beyond any reasonable doubt that galaxies live in dark matter halos – if general relativity is a good description of gravity at those scales. Gravitational lensing (especially strong lensing at sub-galactic scales Treu 2010) provides an additional and powerful tool to shed light on dark matter. By exploiting the deflection of light rays from background sources it need not rely on the presence of luminous tracers in the deflector. Furthermore, gravitational lensing is only sensitive to the total gravitational potential and therefore can provide accurate measurements of mass and mass distribution independent of its dynamical state or nature.

The combination of strong gravitational lensing with other diagnostic tools, such as stellar kinematics (e.g., Miralda-Escude 1995; Natarajan & Kneib 1996; Treu & Koopmans 2002; Koopmans & Treu 2003; Treu & Koopmans 2004; Koopmans et al. 2006, 2009), weak lensing (Gavazzi et al. 2007; Lagattuta et al. 2010), stellar populations synthesis methods (e.g., Grillo et al. 2009; Auger et al. 2009; Thomas et al. 2011; Tortora et al. 2010; Treu et al. 2010; Auger et al. 2010), etc, is particularly effective. By breaking a number of degeneracies inherent to each method alone one can give precise answers to a number of questions. What is the relative abundance of dark and luminous matter in the inner parts of galaxies? Are dark matter density profiles universal as those predicted by simulations? Are halos as triaxal as predicted by simulations? Are there dark satellites around galaxies? How much of the dark matter observed in galaxies is baryonic (i.e. low mass stars and high-mass stars remnants) and how much is non-baryonic?

Until a few years ago, answers to these questions based on strong gravitational lensing where mostly limited by the small samples of known lenses. In fact, strong lensing is a relatively rare phenomenon, and in general only

[1] Institut d'Astrophysique de Paris, UMR7095 CNRS - Université Pierre et Marie Curie, 98bis bd Arago, 75014 Paris, France
[2] Physics department, University of California, Santa Barbara, CA 93106, USA
[3] Oxford University, Astrophysics, Denys Wilkinson Building, Keble Road, Oxford OX1 3RH, UK
[4] KIPAC, P.O. Box 20450, MS29, Stanford, CA 94309, USA
[5] University of Melbourne, Parkville 3010, Victoria, Australia
[†] Alfred P. Sloan Research Fellow

$\sim 1/1000$ massive galaxy will have a background galaxy sufficiently well aligned along the line of sight to produce multiple-images. However, this situation is changing rapidly owing to the dedicated efforts of a number of groups in exploiting massive imaging and spectroscopic surveys to find samples of strong lenses (Browne et al. 2003; Bolton et al. 2006; Marshall et al. 2009; Treu et al. 2011; Brownstein et al. 2012). In the past few years, dedicated searchs using a variety of techniques and wavelenghts have delivered well over 200 galaxy-scale strong lenses.

The Strong Lens Legacy Survey (SL2S Cabanac et al. 2007) is a dedicated effort to find strong lens systems in the Canada-France-Hawaii Telescope Legacy Survey (CFHTLS)[7] with the goal of answering fundamental questions about the distribution of mass and light. It consists of two main efforts: the group and cluster-scale survey (Limousin et al. 2009; More et al. 2011; Verdugo et al. 2011) and this present series that is concerned with the follow-up and analysis of the galaxy-scale sample (Gavazzi et al. 2012, in prep.). The candidates are identified using the `RingFinder` algorithm which detects compact rings around centers of isolated galaxies ($\lesssim 10^{13} M_{\odot}$), and works by focusing on chromatic image excesses around early-type lens galaxies (ETG) that are indicative of the presence of lensed arcs. For each of a sample of pre-selected bright ($i_{\rm AB} \leq 22.5$) red galaxies, a scaled, PSF-matched version of the *i*-band cutout image was subtracted from the *g*-band image of the same system. The rescaling in this operation is performed such that the ETG light is efficiently removed, leaving only objects with a Spectral Energy Distribution different from that of the target galaxy. These typically blue residuals are then characterized with an object detector, and analyzed for their position, ellipticity, and orientation, and those showing characteristic properties of lensed arcs are kept as lens candidates. A sample of several hundred good candidates were visually inspected and ranked for follow-up HST imaging *HST* and *VLT* or *Keck* spectroscopy that are required to confirm their actual lensing nature and to allow accurate lens modeling. The SL2S galaxy-scale sample provides an ideal higher-z complement to the SLACS: the deflectors have similar distribution in size and velocity dispersion, but they have a median redshift of ~ 0.5 (c.f. $z_d \sim 0.2$ for SLACS), extending the baseline for evolutionary studies back to half the current age of the Universe.

In this series we construct lens models for confirmed SL2S galaxy-scale lenses, and interpret them by themselves and in combination with stellar kinematics and stellar population synthesis models (paper II, Ruff et al. 2011). This paper presents lens models for the 16 confirmed systems as well as 1 candidate which proved impossible to model with simple gravitational potentials and was therefore rejected as strong lenses. We use the results to discuss relative orientation of mass and light and their flattening. The companion Paper II discusses the relative abundance of mass and light and the evolution of the mass density profile by combining the SL2S, SLACS, and LSD samples.

This paper is organized as follows. In Section 2 we introduce the CFHT and HST data used in the analysis. In Section 3 we describe our modeling techniques. Section 4 describes the lens models and presents our results on the relative alignment of mass and light. A brief discussion of the properties of the lensed sources is also presented. Section 5 concludes with a brief summary.

Throughout this paper magnitudes are given in the AB system. We assume a concordance cosmology with matter and dark energy density $\Omega_m = 0.3$, $\Omega_\Lambda = 0.7$, and Hubble constant H_0=70 $\mathrm{kms}^{-1}\mathrm{Mpc}^{-1}$.

2. OBSERVATIONS

2.1. *CFHT data*

The CFHTLS consists of two main components of sufficient depth and image quality to be interesting for lens search[8]. Both are imaged in the u*, g, r, i and z bands with the 1 deg^2 field-of-view Megacam Camera. The multi epoch Deep survey covers 4 pointing of 1 deg^2 each. Two different image stacks were produced: D-85 contains the 85% best seeing images whereas the D-25 only includes the 25% best seeing images. For finding lenses we only considered the better resolution stacks. In the T06 data release used for this study they reach a typical depth of $u^* \simeq 26.18$, $g = 25.96 \simeq 25.47$, $r \simeq 25.43$, $i \simeq 25.08$ and $z \simeq 24.57$ (80% completeness for point sources) with typical FWHM point spread functions of $0.''75$, $0.''69$, $0.''64$, $0.''62$ and $0.''61$, respectively. The Wide survey is a single epoch imaging survey, covering some 171 deg^2 in 4 patches of the sky. It reaches a typical depth of $u^* \simeq 25.35$, $g \simeq 25.47$, $r \simeq 24.83$, $i \simeq 24.48$ and $z \simeq 23.60$ (AB mag of 80% completeness limit for point sources) with typical FWHM point spread functions of $0.''85$, $0.''79$, $0.''71$, $0.''64$ and $0.''68$, respectively. Because of the greater area, the Wide component is our main source of lens candidates.

Around each lens and in each CFHTLS band, we produce cutout images 101 pixels (*i.e.* $18.''8$) wide. Nearby stars are used to produce a synthetic PSF model. The 17 systems analyzed in this study are shown in Figure 1 and listed in Table 2.

2.2. *HST follow-up imaging*

In order to confirm the lensing hypothesis and allow for detailed lens modelling, 65 galaxy-scale lens candidates have been observed with the Hubble Space Telescope (HST) as snapshot programs during cycles 15, 16, 17 (GOs 10876, 11289 PI J.-P. Kneib; GO 11588 PI Gavazzi). The observations started with the Advanced Camera for Surveys (ACS), then switched to the Wide Field and Planetary Camera 2 (WFPC2) after the failure of ACS, and finally turned to the Wide Field Camera 3 (WFC3) after Servicing Mission 4. Approximately 50% of the lens candidates were confirmed as lenses in this way. A more comprehensive description of the efficiency of the SL2S lens finding strategy is given by Gavazzi et al.(2012, in preparation).

Ten of the galaxy-scale systems were observed with HST early enough to be included in our first Keck spectroscopic follow-up campaign and are the subject of paper I and II. The remaining systems will be presented in a forthcoming paper at the end of the Keck and HST

---

[7] See `http://www.cfht.hawaii.edu/Science/CFHLS/` and links therein for a comprehensive description

[8] See `http://terapix.iap.fr/cplt/T0006/T0006-doc.pdf` (Goranova et al. 2009)

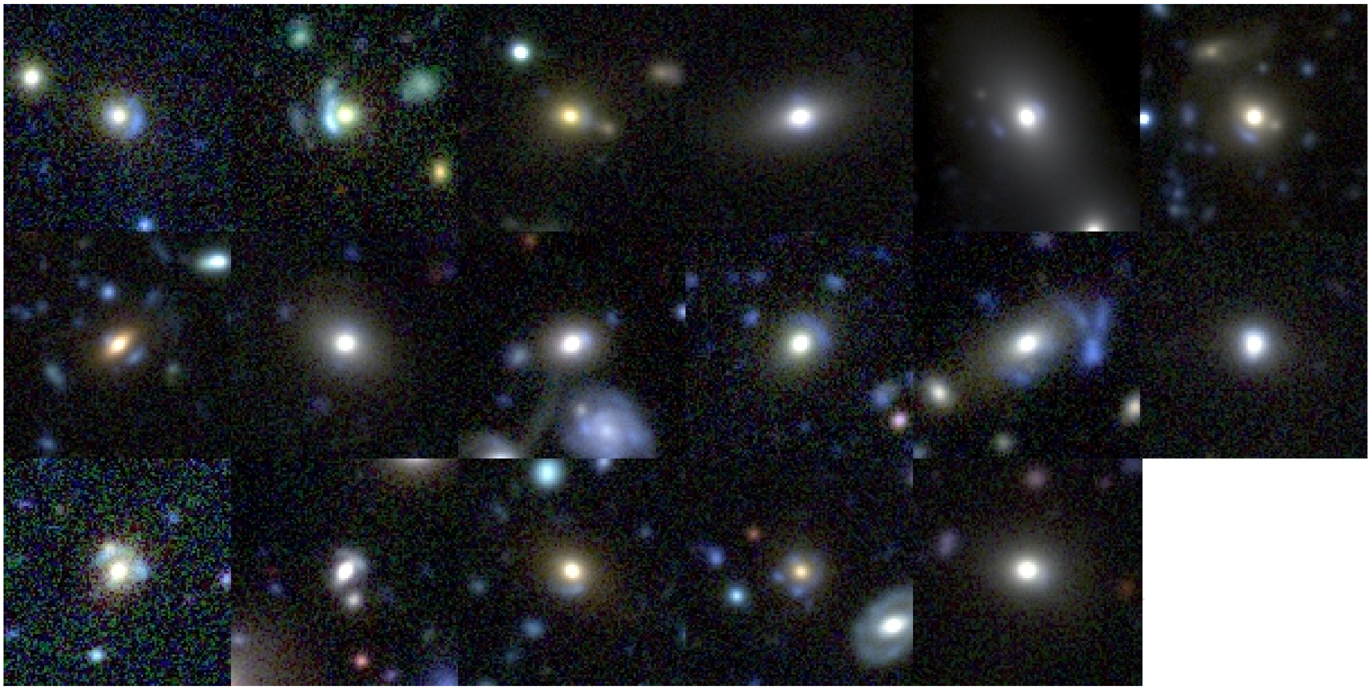

Fig. 1.— Gallery of the 17 SL2S systems studied here (composite rgb color obtained with Megacam g, r and i filters). From top left to bottom right, the lenses are sorted like in table 2. Images are 18.″8 on a size and oriented North up and East left.

TABLE 1
Summary of HST observations.

name	instrument/filter	exp. time (sec)	pixel scale (arcsec)
SL2SJ021411−040502	ACS/F606W	400	0.05
	ACS/F814W	800	0.05
SL2SJ021737−051329	ACS/F606W	400	0.05
	ACS/F814W	800	0.05
SL2SJ022511−045433	WFPC2/F606W	1200	0.1
SL2SJ022610−042011	WFPC2/F606W	1200	0.1
SL2SJ022648−040610	WFPC2/F606W	1200	0.1
SL2SJ023251−040823	WFPC2/F606W	1200	0.1
SL2SJ140123+555705	WFPC2/F606W	1200	0.1
SL2SJ141137+565119	WFC3/F475X	720	0.04
	WFC3/F600LP	720	0.04
SL2SJ221326−000946	WFPC2/F606W	1200	0.1
SL2SJ221407−180712	WFPC2/F606W	1200	0.1

observing campaigns. Of these ten systems, three were observed in two bands, with ACS or WFC3 whereas the others were observed only in a single WFPC2 band as detailed in Table 1.

All the WFPC2 data were reduced using standard `MultiDrizzle`[9] recipes. The cosmic ray removal worked well because the 1200 sec exposure time was split into 3 exposures. The "drizzling" was performed by preserving the CCD frame orientation and pixel scale to avoid producing correlated noise. The ACS and WFC3 observations consisted of single or double exposures only and therefore we relied on `LA-Cosmic` (van Dokkum 2001) on individual exposures for cosmic ray removal, before combining them with `swarp` (Bertin et al. 2002). Like for WFPC2 images are kept in the natural CCD frame. Exposure times and final pixel scales are given in Table 1.

3. MODELING METHODOLOGY

In order to model the light distribution of a galaxy-scale gravitational lens, one has to disentangle the contribution of the foreground deflector and that of the background lensed arc-like features. The former is generally a red ETG and the former a dimmer, blue, and presumably star-forming, more distant source. The light distribution of an ETG generally has a regular shape sufficiently well described by a Sérsic (Sersic 1968) or even a de Vaucouleurs profile (de Vaucouleurs 1948) with very small color gradients and blue background sources are also well represented by Exponential profiles. The separation of these two components is relatively straightforward for ETGs deflectors and they can generally be fitted independently for most applications. However, very detailed investigations of the source properties of high signal-to-noise data might require a simultaneous fit of both components (*e.g.* Marshall et al. 2007), especially with ground-based data (Brault et al., in prep) and bright arcs. We describe our procedure to fit the foreground deflector in 3.1. In Section 3.2 we describe how we use the residual lensed images to model the gravitational potential of the deflector and the intrinsic surface brightness of the source.

3.1. *Foreground deflector*

We used the versatile `galfit` software (Peng et al. 2002) to perform the subtraction of the foreground deflector as it allows to account for boxy-/diskyness of isophotes. It generally yields good image subtraction with a Sérsic profile (see Fig. 4) but the recovered Sérsic indices n and effective radii $R_{\rm eff}$ are quite degenerated and this often leads to misleading values of n and $R_{\rm eff}$. We thus used a generic Sérsic profile to get as good a deflector subtraction as possible and we forced $n = 4$ to get more robust values of n and $R_{\rm eff}$. In the same vein, the fit of the $n = 4$ foreground lens also yields a robust measurement of ellipticity and orientation of the light distribution. These values are reported in table 2.

---

[9] `MultiDrizzle` is a product of the Space Telescope Science Institute, which is operated by AURA for NASA (Koekemoer et al. 2002).

Fits are performed in all the available bands of a given lens using $18\farcs8$ on a side cutout images and suitable PSF either inferred from the neighboring stars or from `TinyTim` (Krist et al. 2011)[10] in the case of HST data. The formal errors on each parameter are generally very small due because they only account for statistical errors and not modelling errors associated with the somewhat over-simplistic assumptions about the light distribution. A more realistic estimate of the total uncertainties on the recovered ellipticity, orientation and effective radius can be made by estimating the filter-to-filter dispersion on these parameters when HST data is missing. When HST imaging is available, shape parameters characterizing the deflector are more robustly measured and we adopt the formal errors from `galfit`.

3.2. *Lensed features and mass modeling*

For lens modeling we used a dedicated code `sl_fit` developed for and tested on galaxy-scale strong lenses (*e.g.* Gavazzi et al. 2007, 2008, 2011; Tu et al. 2009). The code fits model parameters of simple analytic lensing potentials. It uses the full surface brightness distribution observed in the image plane and attempts to explain it with one or more simple analytic light components described by an exponential radial profile with elliptical shape (see *e.g.* Marshall et al. 2007; Bolton et al. 2008, for similar techniques).

The lensing potential is assumed to be made of a singular isothermal ellipsoid (SIE), centered on the main deflector. This is the simplest mass profile that has been shown to yield a description of the mas distribution of massive early-type galaxies sufficient to derive Einstein Radius, position angle and ellipticity (Treu 2010). The convergence profile of the central mass component is given by

$$\kappa(x,y) = \frac{b}{2\xi}, \qquad (1)$$

where the scaling parameter b is the Einstein radius $R_{\rm Ein}$ and is related to the velocity dispersion of the deflector through $b/1'' = (\sigma_v/186.21 \ {\rm km\,s^{-1}})^2 D_{\rm ls}/D_{\rm s}$ and $\xi^2 = qx^2 + y^2/q$ is the radial coordinate that accounts for the ellipsoidal symmetry of the iso-density contours and q is the minor-to-major axis ratio. The orientation of the major axis ${\rm PA_{tot}}$ is allowed to vary, although this is not explicit in the definition of Equ. (1). We do not assume *a priori* that the orientation of the total mass distribution is correlated to that of the observed stellar component. This way the total potential can capture (and mix because of substantial degeneracies) internal and external quadrupolar terms in the potential (Keeton et al. 1997). We also add an external shear parameter when more information is available (see the case of SL2SJ021737-051329 described below), sufficient to break the degeneracy between external shear and orientation of the galaxy potential.

Like in the previous step, when we fitted the foreground light distribution we weigh pixels with the image inverse total variance (including sky, foreground and lensed features). The χ^2 term relating the observed light distribution $I(\vec{x}_i)$ at pixel i and the intrinsic source light distribution $S(\vec{y})$ is thus:

$$\chi^2 = \sum_i \frac{\left[I(\vec{x}_i) - S\left(\vec{x}_i - \vec{\alpha}\left(\vec{x}_i|\vec{p}_{\rm p}\right)|\vec{p}_s\right)\right]^2}{\sigma_i^2} \ , \qquad (2)$$

where $\vec{p}_{\rm p} = [b, q, {\rm PA_{SIE}}]$ contains the parameters that determine the gravitational potential and $\vec{p}_s = [x_{\rm s}, y_{\rm s}, q_{\rm s}, {\rm PA_s}, m_{\rm s}, r_{\rm s}]$ is the section of the parameter space that codes for the source light distribution, namely its center $\vec{x}_s$, its ellipticity $q_{\rm s}$, its orientation ${\rm PA_s}$, its magnitude $m_{\rm s}$ and half-light radius $r_{\rm s}$.

The optimization of these 9 parameters is performed using Monte Carlo Markov Chain techniques. Reported model parameters and confidence intervals are taken from the 0.50, 0.16 and 0.84 quantiles. However, because of the simplicity of both the model potential and model source light distribution, we generally end up with very small formal errors on the recovered model parameters that should be substantially increased. Bolton et al. (2008) estimated that relative errors on $R_{\rm Ein}$ should be about 5%. We thus add this dominant contribution in quadrature to the statistical errors in table 2 and do the same for the axis ratio $q_{\rm SIE}$.

4. RESULTS

In this section we describe the lens model of each system (§ 4.1). In addition, we study the shape and relative orientation of the light and total mass distributions as they do are independent of the source and deflector redshift (§ 4.2). Results depending on spectroscopic information (source and deflector redshifts and velocity dispersion) quantity along with a novel method proposed to mitigate the nuisance due to the ignorance of the source redshift are presented in Paper II.

4.1. *Notes on Individual Lens models*

For each lens in the sample we describe the resulting best fit model:

- SL2SJ021411-040502 is well reproduced by the single SIE potential + Exponential source model. We note a small axis ratio $q_{\rm SIE} \sim 0.33$ this seems at odds with the more circular light distribution $q_* \sim 0.89$. This can be explained by the presence of a neighbor galaxy at the same redshift as $z_{\rm d}$ about $8''$and $PA \sim 65°$ which enhances the elongation of the potential.

- SL2SJ021737-051329 has been studied by in detail by Tu et al. (2009). Our results are in agreement with theirs. A simple SIE + Exponential source yields a good fit, even though a better fit is achieved by introducing both internal ellipticity through the SIE potential and external shear (consistent with the presence of a nearby group of galaxies). Similar conclusions were recently found by Cooray et al. (2011) using additional Near IR CANDELS data. The source redshift is $z_{\rm s} = 1.847$ (Paper II). This implies that the source half-light radius is $R_{\rm eff,s} = 0\farcs081^{+0.028}_{-0.016} \simeq 0.69^{+0.24}_{-0.13}\,{\rm kpc}$ for an F606W magnitude $m_{\rm s} = 24.45 \pm 0.10$. The system is lensing a second source at $z_{s2} \sim 2.3$ that

---

[10] `http://www.stsci.edu/hst/observatory/focus/TinyTim`

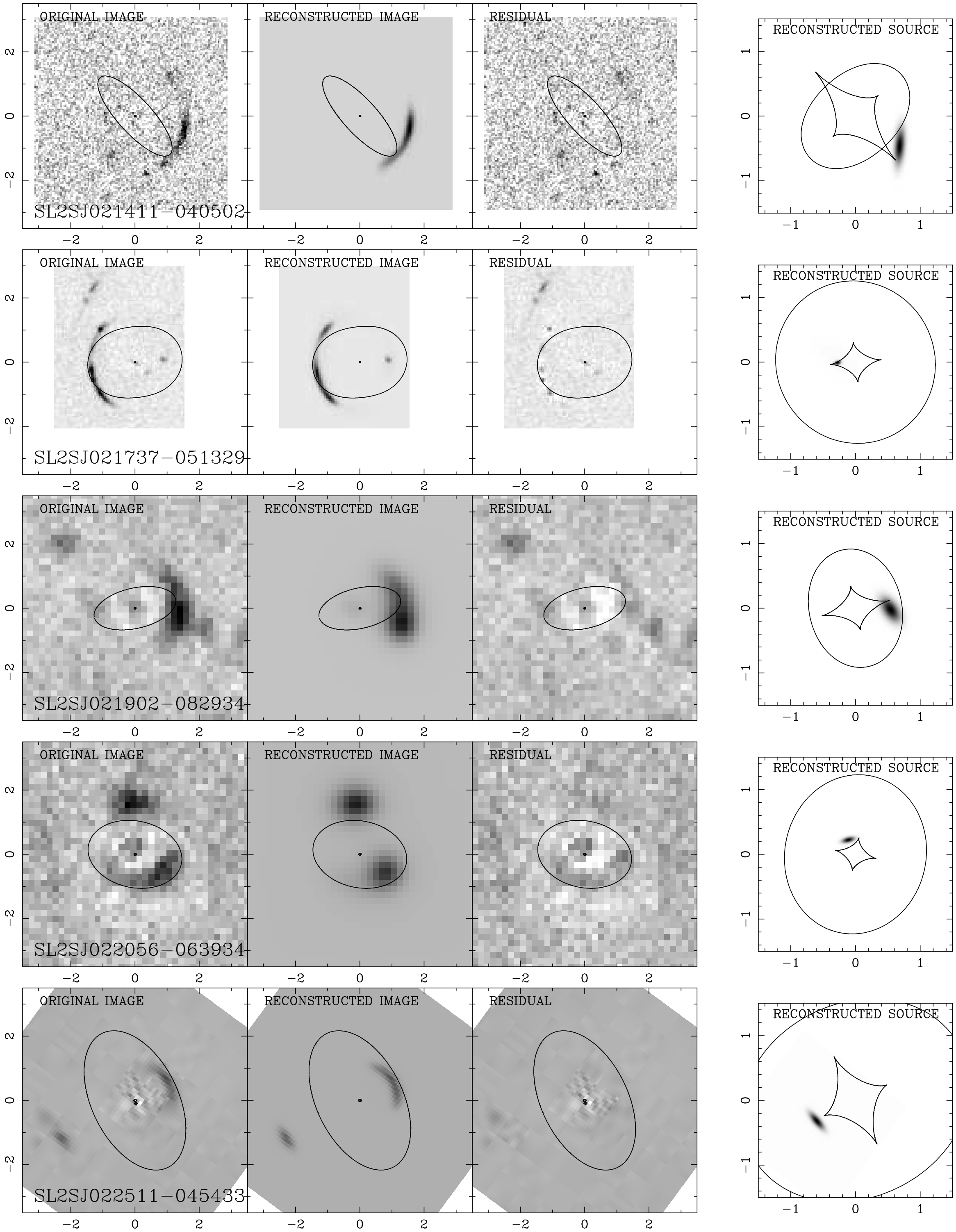

FIG. 2.— Results of the lens modeling analysis. For each row, a system is shown with, from left to right, lensed features with the deflector subtracted off with `galfit` (data), the best fit model prediction (model), the residual (data-model) and the associated source plane light distribution. The critical lines are overlaid in the first three panels whereas the caustics lines are shown in the last one.

we do not consider here for consistency with the other systems. However, regardless of whether the second source is modelled or not, the good signal-to-noise ratio and the favorable image configuration allows us to break the degeneracy between external shear and internal ellipticity and we therefore get constraints on both. We find an external shear $\gamma_{\rm ext} = 0.064 \pm 0.003$ with an orientation $\mathrm{PA}_{\rm ext} = 89.^{\circ}7 \pm 0.^{\circ}4$. We see that the light is well aligned with the external shear and about ~ 33 deg misaligned with the SIE component. This may be due to tidal effects.

- SL2SJ021902-082934 is another ”cusp” configuration with a marginal candidate counter image on the opposite side. The lack of HST imaging im-

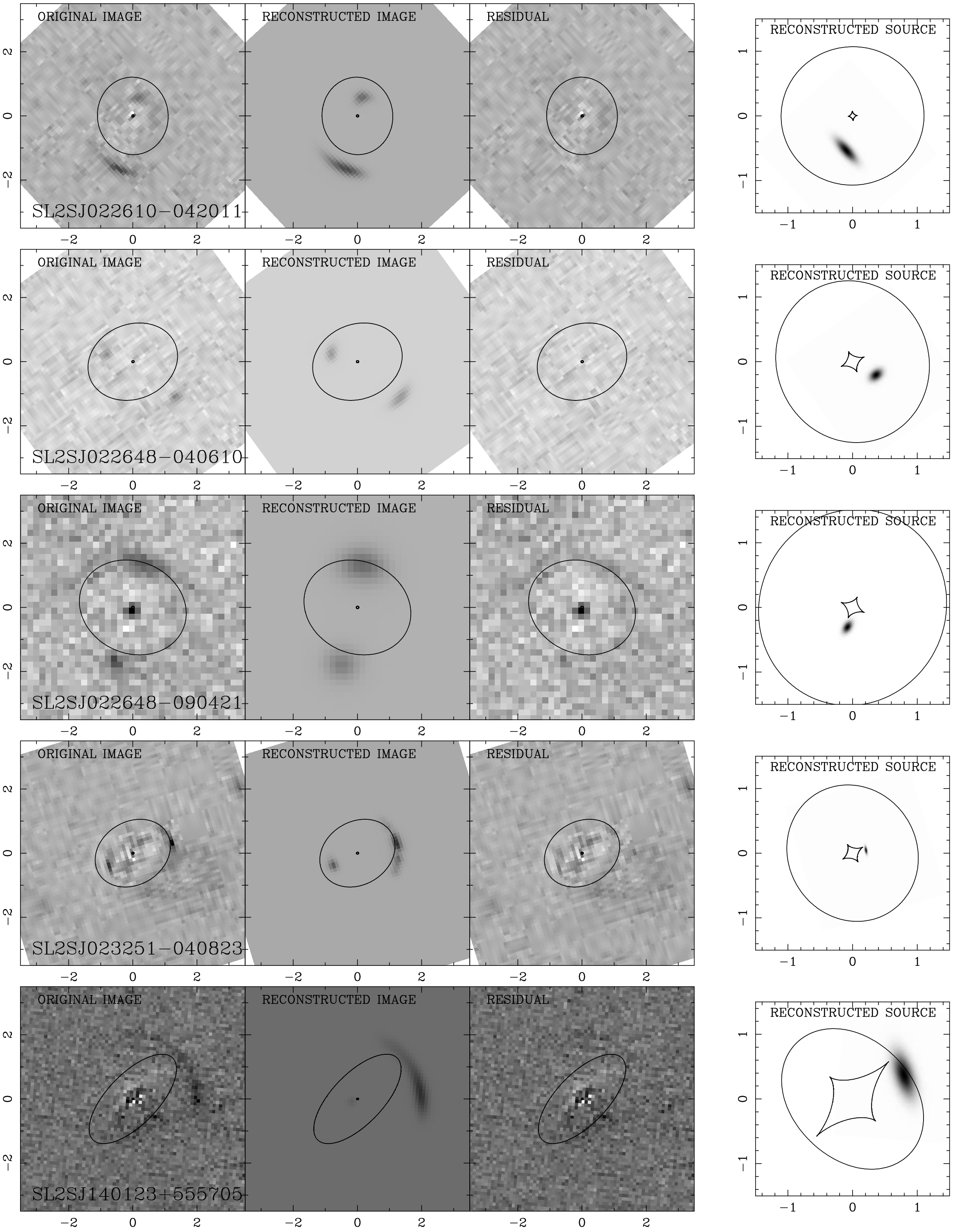

FIG. 3.— Lens models (continued).

plies that we had to consider the CFHT g band image. We can see an additional source westward of the arc that has a color similar of the deflector and should not be considered as a lensed feature. Since we can achieve a good fit of the arc without introducing this perturbation we neglect it.

- SL2SJ022056-063934 is a minor axis cusp configuration. The single source component does not perfectly capture the faint tail of the inner arc although most of the flux is well recovered, even with ground-based resolution.

- SL2SJ022511-045433 is a low redshift bright deflector with another bright minor axis cups configuration. The source redshift is $z_{\rm s} = 1.199$ (paper II). We report here the result with a single source component of magnitude $m_s = 24.14 \pm 0.04$

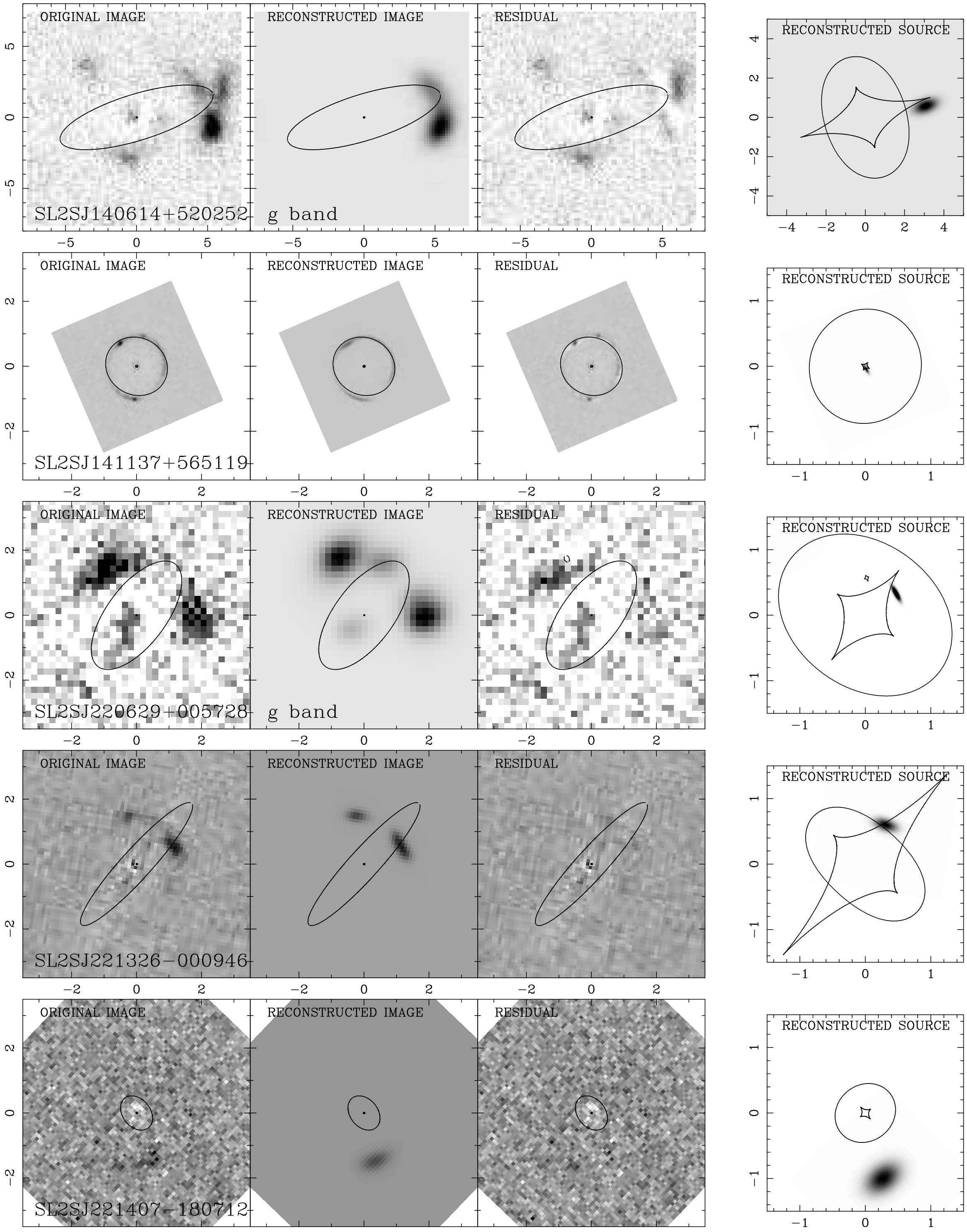

FIG. 4.— Lens models (continued). Note the different plotting range for the first row corresponding to SL2SJ140614+520252.

in the F606W band and half-light radius $R_{\rm eff,s} = 0\farcs125 \pm 0\farcs003 \simeq 1.037 \pm 0.025\,$kpc. We note we also attempted to account for the fainter extension of the furthest arc (on the East of the deflector), with a secondary component. This would even lower the residuals on the two multiple images without changing the results on the recovered potential parameters. Accounting for this component the source would be ~ 0.36 magnitudes brighter.

- SL2SJ022610-042011 is a typical large impact parameter double configuration implying a substantial differential magnification of the two multiple images. In addition, these two are nearly aligned with the center of the deflector. This is consistent with the potential being close to circularly symmetric ($q_{\rm SIE} \sim 0.92$). This system has a known source redshift $z_{\rm s} = 1.232$. We can thus estimate the source half-light radius $R_{\rm eff,s} = 0\farcs160 \pm 0\farcs011 \simeq$

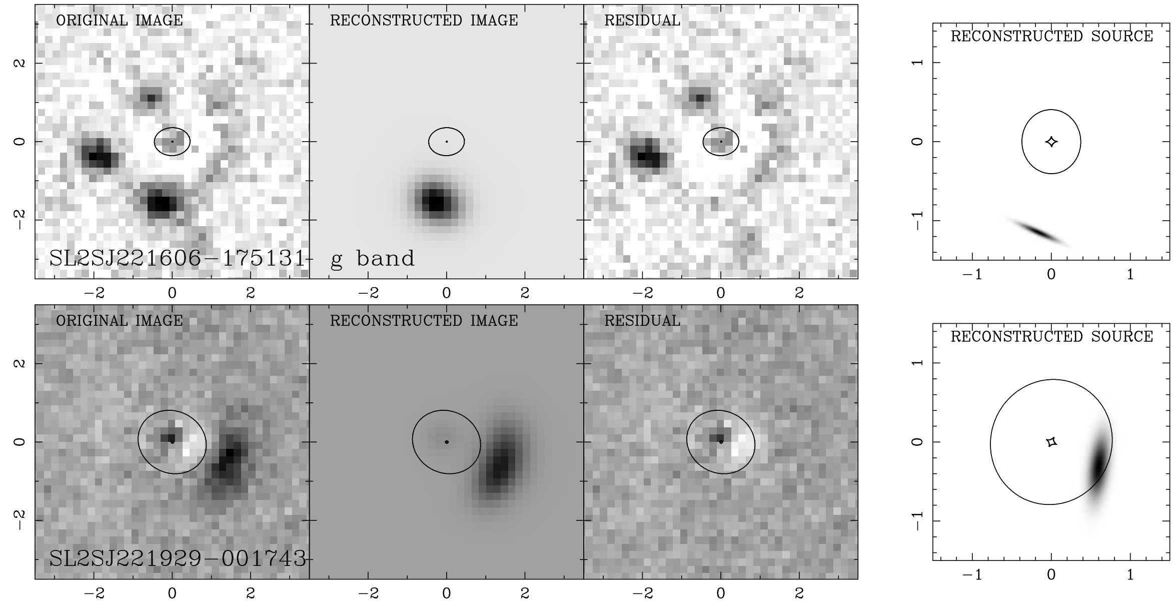

Fig. 5.— Lens models (continued). Note that the system in the first row, SL2SJ221606-175131, is not a satisfying model of a lens and we disqualify it as being an actual gravitational lens.

$1.332 \pm 0.092\,$kpc for an F606W magnitude $m_{\rm s} = 25.10 \pm 0.08$.

- SL2SJ022648-040610 is another double configuration with a more balanced magnification ratio between the two images involving a slightly more elongated potential. We notice that the deflector looks like an edge-on S0 galaxy with an elongated light distribution. However, the total potential is considerably more circular.

- SL2SJ022648-090421 is also modeled using Megacam g band data and shows a minor axis cusp configuration with little deviation between light and SIE orientations. This is the faintest source we reconstruct with $m_{\rm s} = 27.13 \pm 0.14$.

- SL2SJ023251-040823 is a double system with the source close to the cusp.

- SL2SJ140123+555705 shows a dim cusp-like arc. Even though we cannot identify the counterimage, the substantial bending of the arc breaks the degeneracy between shear and intrinsic source ellipticity and allows us to measure the Einstein radius with good accuracy $R_{\rm Ein} = 1\farcs19 \pm 0\farcs07$, comparable to the other cases.

- SL2SJ140614+520252 is another cusp configuration on a larger scale, as $R_{\rm Ein} = 3\farcs02 \pm 0\farcs15$. Some blue light excesses are seen in the g band image shown the Fig. 4 and only the main “naked” cusp arc is captured by our model. However we can see that the other Western component is not multiply imaged as the source would fall outside the caustic. Thus it does not provide more information and we verified that its inclusion does not change our conclusions on the lensing potential. Even by ignoring this second singly imaged source component, we find that this system involves the brightest source of the sample with g band $m_{\rm s} = 23.50 \pm 0.03$. We could not find a solution with a lensed source reproducing the Southern and Northeastern blue excesses. The lens potential is highly elongated with $q_{\rm SIE} = 0.290 \pm 0.015$. This is potentially due in part to shear from a galaxy about $8\farcs3$ in the South East direction.

- SL2SJ141137+565119 is the only system having WFC3 imaging presented here. The signal-to-noise ratio is good and allows us to get tight constraints on the potential and on the source whose redshift is found to be $z_{\rm s} = 1.420$. The source half-light radius in the F475X band is $R_{\rm eff,s} = 0\farcs058 \pm 0\farcs001 \simeq 0.490 \pm 0.008\,$kpc and its magnitude is $m_{\rm s} = 25.86 \pm 0.04$. We note that the addition of a very compact core would improve the fit further as our single source component does not reproduce the full complexity of the source light distribution. Our best fit model nevertheless captures most of the extended Einstein ring.

- SL2SJ220629+005728 is modeled using the g band Megacam image. However, we see in Fig. 1 that a small red satellite lies on top of the lensed blue features. We thus need to disentangle both contributions by simultaneously fitting to the g and i bands one lensed source and one foreground unlensed source centered in the red satellite. This satellite also contributes to the lens potential through a point mass component of unknown mass. We find that this perturbing mass has to be $M_{\rm pert} \leq 2 \times 10^9\,M_\odot$ (68% CL). Getting HST imaging data would significantly improve the accuracy of the decomposition and the constraints on $M_{\rm pert}$. The Einstein radius estimate is robust with respect to the inclusion (or not) of the perturbing potential.

- SL2SJ221326-000946 is an edge-on disk galaxy in which both the potential and the light distribution are highly elongated: $q_{\rm SIE} = 0.191 \pm 0.014$ and

$q_* = 0.277 \pm 0.007$ with a small $\Delta\mathrm{PA} \sim 10^{\circ}.4 \pm 0^{\circ}.6$ misalignment.

- SL2SJ221407-180712 does not exhibit any counter-image nor a strong curvature of the main outer image. This implies that the model cannot be constrained well and we can only place upper limits on the Einstein Radius $R_{\mathrm{Ein}} = 0.^{\prime\prime}41 \pm 0.^{\prime\prime}23$. The results on the potential elongation and orientation are thus very loose and we do not consider this system in the statistical analysis of §4.2. Note that the small upper limit on R_{Ein} is consistent with other mass constraints in paper II.

- SL2SJ221606-175131 has a relatively symmetric configuration. Its similarity to a classic quad configuration lead us to include it in the lens candidate sample. However, we could not find any sensible lens model able to reproduce in detail the image configuration. Therefore we conclude that this system is not a lens, or more precisely, that the blue features about $1^{\prime\prime}$ from the center of the ETG do not originate from a unique background source. We speculate tha it could be due to low surface brightness star formation at the ETG's redshift. We thus exclude this system from the statistical analysis below.

- SL2SJ221929-001743 does not have HST imaging and the CFHT data do not allow us to constraint tightly the potential parameters as we cannot identify unambiguously a counterimage. In addition, the arc does not display a strong curvature at the resolution of ground-based imaging. We thus get weaker constraints on the Einstein Radius $R_{\mathrm{Ein}} = 0.^{\prime\prime}74 \pm 0.^{\prime\prime}14$ than for other systems. HST imaging would significantly improve the mass model. Given the redshift of the source $z_{\mathrm{s}} = 1.023$, we infer a source half-light radius $R_{\mathrm{eff,s}} = 0.^{\prime\prime}384^{+0.073}_{-0.054} \simeq 3.03^{+0.59}_{-0.43}$ kpc and a g band intrinsic magnitude $m_{\mathrm{s}} = 24.08 \pm 0.21$.

4.2. *Alignment of mass and light*

The top panel of Figure 6 compares the ellipticity of the stellar component to that of the mass model. For the vast majority of the objects the ellipticities are tightly correlated. This is expected since stellar mass makes up a significant fraction of the total mass within the Einstein Radius. However, there are few interesting outliers. The flattened light distribution of SL2SJ022648-040610 is consistent with a disky galaxy living in significantly rounder halo. Perhaps more suprising are the cases of SL2SJ021411-040502 and SL2SJ220629+005728, where the stars are almost round, while the potential is significantly flattened. In both cases the source of the ellipticity of the mass distribution seems to be external shear, associated with a satellite. In general, the relation between light and mass ellipticity seems to have significantly more scatter than that found for the SLACS sample, $< q_{\mathrm{SIE}}/q_* >= 0.95$ with scatter 0.48, as opposed to 0.99 with scatter 0.11 (Koopmans et al. 2006). As we discuss in the next paragraph this is probably due to a much more significant role played by external shear. The bottom panel of Figure 6 shows the angular offset between light and mass PA as a function of mass ellipticity. Even neglecting the points with $q_{\mathrm{SIE}} > 0.85$, where clearly the position angle is not very well measured since the potential is so circular, there is considerable scatter around zero. For the entire sample the rms scatter is 25 degrees, while if we limit ourselves to $q_{\mathrm{SIE}} < 0.85$ the scatter is still 18 degrees. Again this is considerable higher than the 10 degrees found for the SLACS sample (Koopmans et al. 2006) in general, and closer to the values found for the subset of SLACS lenses that reside in overdense environments (Treu et al. 2009). A simple calculation, based on Eq 22 in the paper by Keeton et al. (1997) and assuming that the direction of external shear is randomly distributed with respect to that of the mass of the galaxies shows that this is consistent with a relatively large average external shear. This is illustrated in Figure 7 where we show the expected r.m.s. fluctuation of the position angles as a function of average external shear. Regardless of whether the rounder objects are included or not, it seems that external shear of order ≈ 0.12 is required on average. This level of external shear is fairly common amongst galaxy-scale gravitational lenses (e.g. Keeton et al. 1997; Holder & Schechter 2003), and it is likely due to the environment of the lenses (Auger et al. 2007; Treu et al. 2009; Auger 2008; Wong et al. 2011), since massive early-type galaxies typically reside at the centers of groups. The lower level of external shear in the SLACS sample is most likely due to the smaller size of their Einstein radius relative to the characteristic scale of the galaxy (half effective radius typically), and therefore the more relevant role played by stellar mass in defining the potential within the critical curve. We note also that, despite a greater influence of the environment relative to SLACS, the SL2S lenses do not require as large an quadrupolar term as JVAS radio source or quasars (Keeton et al. 1997). This might be due to the fact that extended sources are not as sensitive to the magnification bias that would boost the fraction of highly magnified quads. In turn, the only unambiguous quad

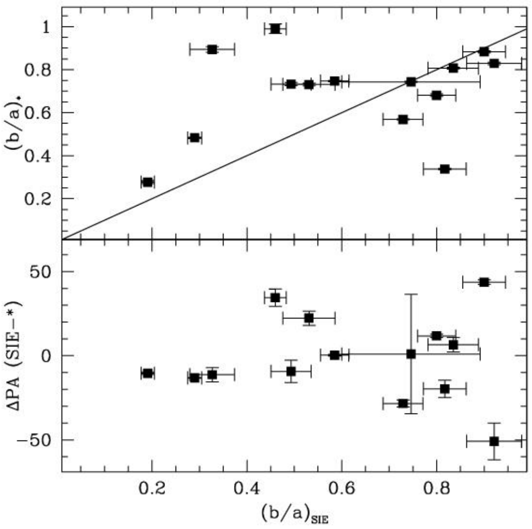

FIG. 6.— Top panel: correlation between axis ratio of the light and of the mass distribution. Bottom panel: angular offset between the major axis of the mass distribution and that of the light as a function of axis ratio of the mass distribution. SL2SJ021737−051329 is not included because this system was modeled including external shear.

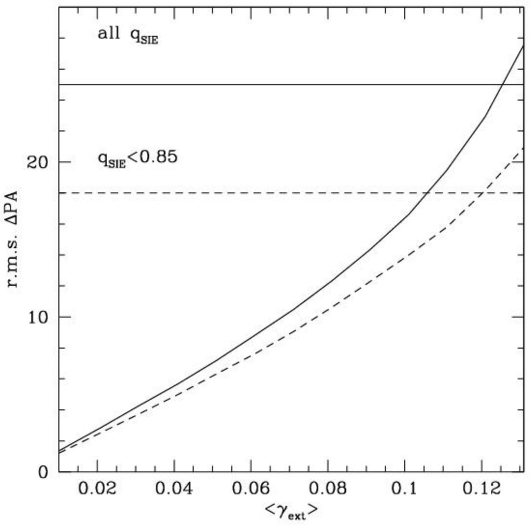

FIG. 7.— The curves represent the expected rms fluctuations of the offset in PA as a function of average external shear. The horizontal lines represent the values measured for the SL2S sample. The solid lines refer to the whole sample, while the dashed lines refer to the subsample with mass axis ratio $q_{\rm SIE} < 0.85$.

systems here are J141137+565119 and J021737−051329. Two out of 16 lenses (excluding J221606−175131) are quads.

5. SUMMARY

In this paper we have presented gravitational lens models of a pilot sample of 16 galaxy-scale lenses identified as part of the SL2S Survey. Hubble Space Telescope imaging is available for 10/16 systems, while for the others the modelling is based on ground based CFHTLS imaging. After removing the light from the foreground deflector we use the surface brightness distribution of the background source to constrain mass models of the deflector galaxy. For each system we derive Einstein Radius, position angle and ellipticity of the mass distribution described as a singular isothermal ellipsoid. These parameters are used in paper II in combination with spectroscopic information to study the relative distribution of stellar and dark matter in early-type galaxies and its evolution with cosmic time. In this paper we focus on the relative orientation and ellipticity of the luminous and total mass distribution, which does not require spectroscopic information. We find that ellipticity of mass and light are tightly correlated except for a handful of outliers. In one case the presence of a disk makes the light distribution significantly flatter than the overall mass distribution. In two cases, the presence of a nearby galaxy introduces significant external shear in the overall mass distribution. In addition, we find that the position angle of mass and light is on average aligned, albeit with r.m.s. scatter of 18-25 degrees, significantly larger than what is found for the lower redshift SLAC sample. We interpret this scatter as evidence for substantial external shear, on average $\langle\gamma_{\rm ext}\rangle \approx 0.12$, resulting from the environment (physically related to the main deflector galaxy or along the line of sight) The physical scale of the SL2S Einstein radii is greater that for SLACS: $R_{\rm Ein}/R_{\rm eff} \simeq 1.1$ vs 0.5 for SLACS (Auger et al. 2010). In addition, we find only two quad lenses in this pilot sample, suggesting that magnification bias is less effective in boosting the statistics of extended lensed sources as compared with samples comprising point sources. Another difference between SL2S and other samples is that SL2S is a deflector selected sample, as opposed to source selected samples like CLASS.

In paper II we combine our lensing information with stellar kinematics to infer the cosmic evolution of the mass density profile of massive galaxies. Given the sample size in paper II, the role of environment and external shear cannot be explored further, neither in terms of astrophysical signal, nor in terms of systematic uncertainty on the mass density slope. However, the follow-up imaging and spectroscopy of SL2S candidates is still ongoing and we plan to investigate these issues with a much larger sampe in future papers of this series. The parallel effort of measuring the redshift of sources with Keck and XShooter on VLT will also allow us to explore the population of lensed sources with greater detail.

RG and FB were supported by the Centre National des Etudes Spatiales. PJM was given support by the TABASGO foundation in the form of a research fellowship. TT acknowledges support from the NSF through CAREER award NSF-0642621, and from the Packard Foundation through a Packard Fellowship. Based on observations obtained with MegaPrime/MegaCam, a joint project of CFHT and CEA/DAPNIA, at the Canada-France-Hawaii Telescope (CFHT) which is operated by the National Research Council (NRC) of Canada, the Institut National des Sciences de l'Univers of the Centre National de la Recherche Scientifique (CNRS) of France, and the University of Hawaii. This work is based in part on data products produced at TERAPIX and the Canadian Astronomy Data Centre as part of the Canada-France-Hawaii Telescope Legacy Survey, a collaborative project of NRC and CNRS. This research is supported by NASA through Hubble Space Telescope programs GO-10876, GO-11289, GO-11588, and in part by the National Science Foundation under Grant No. PHY99-07949, and is based on observations made with the NASA/ESA Hubble Space Telescope and obtained at the Space Telescope Science Institute, which is operated by the Association of Universities for Research in Astronomy, Inc., under NASA contract NAS 5-26555, and at the W.M. Keck Observatory, which is operated as a scientific partnership among the California Institute of Technology, the University of California and the National Aeronautics and Space Administration. The Observatory was made possible by the generous financial support of the W.M. Keck Foundation. The authors wish to recognize and acknowledge the very significant cultural role and reverence that the summit of Mauna Kea has always had within the indigenous Hawaiian community. We are most fortunate to have the opportunity to conduct observations from this mountain.

REFERENCES

Auger, M. W. 2008, MNRAS, 383, L40

Auger, M. W., Fassnacht, C. D., Abrahamse, A. L., Lubin, L. M., & Squires, G. K. 2007, AJ, 134, 668

Auger, M. W., Treu, T., Bolton, A. S., Gavazzi, R., Koopmans, L. V. E., Marshall, P. J., Bundy, K., & Moustakas, L. A. 2009, ApJ, 705, 1099

Auger, M. W., Treu, T., Bolton, A. S., Gavazzi, R., Koopmans, L. V. E., Marshall, P. J., Moustakas, L. A., & Burles, S. 2010, ApJ, 724, 511

Bertin, E., Mellier, Y., Radovich, M., Missonnier, G., Didelon, P., & Morin, B. 2002, in Astronomical Society of the Pacific Conference Series, Vol. 281, Astronomical Data Analysis Software and Systems XI, ed. D. A. Bohlender, D. Durand, & T. H. Handley, 228

Blumenthal, G. R., Faber, S. M., Flores, R., & Primack, J. R. 1986, ApJ, 301, 27

Bolton, A. S., Burles, S., Koopmans, L. V. E., Treu, T., Gavazzi, R., Moustakas, L. A., Wayth, R., & Schlegel, D. J. 2008, ApJ, 682, 964

Bolton, A. S., Burles, S., Koopmans, L. V. E., Treu, T., & Moustakas, L. A. 2006, ApJ, 638, 703

Browne, I. W. A., et al. 2003, MNRAS, 341, 13

Brownstein, J. R., Bolton, A. S., Schlegel, D. J., Eisenstein, D. J., Kochanek, C. S., Connolly, N., Maraston, C., Pandey, P., Seitz, S., Wake, D. A., Wood-Vasey, W. M., Brinkmann, J., Schneider, D. P., & Weaver, B. A. 2012, ApJ, 744, 41

Cabanac, R. A., Alard, C., Dantel-Fort, M., Fort, B., Gavazzi, R., Gomez, P., Kneib, J. P., Le Fèvre, O., Mellier, Y., Pello, R., Soucail, G., Sygnet, J. F., & Valls-Gabaud, D. 2007, A&A, 461, 813

Cooray, A., Fu, H., Calanog, J., Wardlow, J. L., Chiu, A., Kim, S., Smidt, J., Acquaviva, V., Ferguson, H. C., Faber, S. M., Galametz, A., Grogin, N. A., Hartley, W., Kocevski, D., Koekemoer, A., Koo, D. C., Lucas, R. A., Moustakas, L., & Newman, J. A. 2011, ArXiv e-prints

de Vaucouleurs, G. 1948, Annales d'Astrophysique, 11, 247

Duffy, A. R., Schaye, J., Kay, S. T., Dalla Vecchia, C., Battye, R. A., & Booth, C. M. 2010, MNRAS, 405, 2161

Franx, M., van Gorkom, J. H., & de Zeeuw, T. 1994, ApJ, 436, 642

Gavazzi, R., Cooray, A., Conley, A., Aguirre, J. E., Amblard, A., Auld, R., Beelen, A., Blain, A., Blundell, R., Bock, J., Bradford, C. M., Bridge, C., Brisbin, D., Burgarella, D., Chanial, P., Chapin, E., Christopher, N., Clements, D. L., Cox, P., Djorgovski, S. G., Dowell, C. D., Eales, S., Earle, L., Ellsworth-Bowers, T. P., Farrah, D., Franceschini, A., Fu, H., Glenn, J., González Solares, E. A., Griffin, M., Gurwell, M. A., Halpern, M., Ibar, E., Ivison, R. J., Jarvis, M., Kamenetzky, J., Kim, S., Krips, M., Levenson, L., Lupu, R., Mahabal, A., Maloney, P. D., Maraston, C., Marchetti, L., Marsden, G., Matsuhara, H., Mortier, A. M. J., Murphy, E., Naylor, B. J., Neri, R., Nguyen, H. T., Oliver, S. J., Omont, A., Page, M. J., Papageorgiou, A., Pearson, C. P., Pérez-Fournon, I., Pohlen, M., Rangwala, N., Rawlings, J. I., Raymond, G., Riechers, D., Rodighiero, G., Roseboom, I. G., Rowan-Robinson, M., Schulz, B., Scott, D., Scott, K. S., Serra, P., Seymour, N., Shupe, D. L., Smith, A. J., Symeonidis, M., Tugwell, K. E., Vaccari, M., Valiante, E., Valtchanov, I., Verma, A., Vieira, J. D., Vigroux, L., Wang, L., Wardlow, J., Wiebe, D., Wright, G., Xu, C. K., Zeimann, G., Zemcov, M., & Zmuidzinas, J. 2011, ApJ, 738, 125

Gavazzi, R., Treu, T., Koopmans, L. V. E., Bolton, A. S., Moustakas, L. A., Burles, S., & Marshall, P. J. 2008, ApJ, 677, 1046

Gavazzi, R., Treu, T., Rhodes, J. D., Koopmans, L. V. E., Bolton, A. S., Burles, S., Massey, R. J., & Moustakas, L. A. 2007, ApJ, 667, 176

Gerhard, O., Kronawitter, A., Saglia, R. P., & Bender, R. 2001, AJ, 121, 1936

Gnedin, O. Y., Kravtsov, A. V., Klypin, A. A., & Nagai, D. 2004, ApJ, 616, 16

Goranova, Y., Hudelot, P., Magnard, F., McCracken, H., Mellier, Y., Monnerville, M., Schultheis, M., Sémah, G., Cuillandre, J.-C., & Aussel, H. 2009, The CFHTLS T0006 Release

Grillo, C., Gobat, R., Lombardi, M., & Rosati, P. 2009, A&A, 501, 461

Holder, G. P., & Schechter, P. L. 2003, ApJ, 589, 688

Humphrey, P. J., Buote, D. A., Gastaldello, F., Zappacosta, L., Bullock, J. S., Brighenti, F., & Mathews, W. G. 2006, ApJ, 646, 899

Keeton, C. R., Kochanek, C. S., & Seljak, U. 1997, ApJ, 482, 604

Koekemoer, A. M., Fruchter, A. S., Hook, R. N., & Hack, W. 2002, in The 2002 HST Calibration Workshop : Hubble after the Installation of the ACS and the NICMOS Cooling System, ed. S. Arribas, A. Koekemoer, & B. Whitmore, p337

Komatsu, E., Smith, K. M., Dunkley, J., Bennett, C. L., Gold, B., Hinshaw, G., Jarosik, N., Larson, D., Nolta, M. R., Page, L., Spergel, D. N., Halpern, M., Hill, R. S., Kogut, A., Limon, M., Meyer, S. S., Odegard, N., Tucker, G. S., Weiland, J. L., Wollack, E., & Wright, E. L. 2011, ApJS, 192, 18

Koopmans, L. V. E., Bolton, A., Treu, T., Czoske, O., Auger, M. W., Barnabè, M., Vegetti, S., Gavazzi, R., Moustakas, L. A., & Burles, S. 2009, ApJ, 703, L51

Koopmans, L. V. E., & Treu, T. 2003, ApJ, 583, 606

Koopmans, L. V. E., Treu, T., Bolton, A. S., Burles, S., & Moustakas, L. A. 2006, ApJ, 649, 599

Krist, J. E., Hook, R. N., & Stoehr, F. 2011 in (SPIE, Optical Modeling and Performance Predictions V), 81270J

Lagattuta, D. J., Fassnacht, C. D., Auger, M. W., Marshall, P. J., Bradač, M., Treu, T., Gavazzi, R., Schrabback, T., Faure, C., & Anguita, T. 2010, ApJ, 716, 1579

Limousin, M., Cabanac, R., Gavazzi, R., Kneib, J.-P., Motta, V., Richard, J., Thanjavur, K., Foex, G., Pello, R., Crampton, D., Faure, C., Fort, B., Jullo, E., Marshall, P., Mellier, Y., More, A., Soucail, G., Suyu, S., Swinbank, M., Sygnet, J.-F., Tu, H., Valls-Gabaud, D., Verdugo, T., & Willis, J. 2009, A&A, 502, 445

Loeb, A., & Weiner, N. 2011, Physical Review Letters, 106, 171302

Marshall, P. J., Hogg, D. W., Moustakas, L. A., Fassnacht, C. D., Bradač, M., Schrabback, T., & Blandford, R. D. 2009, ApJ, 694, 924

Marshall, P. J., et al. 2007, ApJ, 671, 1196

Miralda-Escude, J. 1995, ApJ, 438, 514

More, A., Cabanac, R., More, S., Alard, C., Limousin, M., Kneib, J.-P., Gavazzi, R., & Motta, V. 2011, ArXiv e-prints

Natarajan, P., & Kneib, J.-P. 1996, MNRAS, 283, 1031

Peng, C. Y., Ho, L. C., Impey, C. D., & Rix, H.-W. 2002, AJ, 124, 266

Perlmutter, S., Aldering, G., Goldhaber, G., Knop, R. A., Nugent, P., Castro, P. G., Deustua, S., Fabbro, S., Goobar, A., Groom, D. E., Hook, I. M., Kim, A. G., Kim, M. Y., Lee, J. C., Nunes, N. J., Pain, R., Pennypacker, C. R., Quimby, R., Lidman, C., Ellis, R. S., Irwin, M., McMahon, R. G., Ruiz-Lapuente, P., Walton, N., Schaefer, B., Boyle, B. J., Filippenko, A. V., Matheson, T., Fruchter, A. S., Panagia, N., Newberg, H. J. M., Couch, W. J., & The Supernova Cosmology Project. 1999, ApJ, 517, 565

Riess, A. G., Filippenko, A. V., Challis, P., Clocchiatti, A., Diercks, A., Garnavich, P. M., Gilliland, R. L., Hogan, C. J., Jha, S., Kirshner, R. P., Leibundgut, B., Phillips, M. M., Reiss, D., Schmidt, B. P., Schommer, R. A., Smith, R. C., Spyromilio, J., Stubbs, C., Suntzeff, N. B., & Tonry, J. 1998, AJ, 116, 1009

Ruff, A. J., Gavazzi, R., Marshall, P. J., Treu, T., Auger, M. W., & Brault, F. 2011, ApJ, 727, 96

Saglia, R. P., Bertin, G., & Stiavelli, M. 1992, ApJ, 384, 433

Sersic, J. L. 1968

Spergel, D. N., & Steinhardt, P. J. 2000, Physical Review Letters, 84, 3760

Thomas, J., Saglia, R. P., Bender, R., Thomas, D., Gebhardt, K., Magorrian, J., Corsini, E. M., Wegner, G., & Seitz, S. 2011, MNRAS, 415, 545

Tortora, C., Napolitano, N. R., Romanowsky, A. J., & Jetzer, P. 2010, ApJ, 721, L1

Treu, T. 2010, ARA&A, 48, 87

Treu, T., Auger, M. W., Koopmans, L. V. E., Gavazzi, R., Marshall, P. J., & Bolton, A. S. 2010, ApJ, 709, 1195

Treu, T., Dutton, A. A., Auger, M. W., Marshall, P. J., Bolton, A. S., Brewer, B. J., Koo, D., & Koopmans, L. V. E. 2011, ArXiv e-prints

Treu, T., Gavazzi, R., Gorecki, A., Marshall, P. J., Koopmans, L. V. E., Bolton, A. S., Moustakas, L. A., & Burles, S. 2009, ApJ, 690, 670

Treu, T., & Koopmans, L. V. E. 2002, ApJ, 575, 87

—. 2004, ApJ, 611, 739

Tu, H., Gavazzi, R., Limousin, M., Cabanac, R., Marshall, P. J., Fort, B., Treu, T., Péllo, R., Jullo, E., Kneib, J., & Sygnet, J. 2009, A&A, 501, 475

van Dokkum, P. G. 2001, PASP, 113, 1420

Verdugo, T., Motta, V., Muñoz, R. P., Limousin, M., Cabanac, R., & Richard, J. 2011, A&A, 527, A124

White, S. D. M., & Rees, M. J. 1978, MNRAS, 183, 341
Wong, K. C., Keeton, C. R., Williams, K. A., Momcheva, I. G., & Zabludoff, A. I. 2011, ApJ, 726, 84

TABLE 2
Summary of key observables.

name	z_d	m_i (AB)	input	R_Eff (arcsec)	R_Ein (arcsec)	q_SIE	PA_SIE	q_*	PA_*	source mag
SL2SJ021411−040502	0.609	18.78	ACS/F606W	0.94 ± 0.05	0.92 ± 0.07	0.33 ± 0.05	42.3 ± 1.3	0.89 ± 0.02	53.6 ± 4.0	24.30 ± 0.12
SL2SJ021737−051329	0.646	19.47	ACS/F606W	0.77 ± 0.04	1.27 ± 0.06	0.91 ± 0.05	124.3 ± 2.4	0.92 ± 0.02	91.2 ± 4.5	24.45 ± 0.10
SL2SJ021902−082934	0.390	19.33	Megacam/g	0.90 ± 0.08	0.92 ± 0.06	0.53 ± 0.05	102.0 ± 4.1	0.73 ± 0.01	79.7 ± 1.0	25.35 ± 0.19
SL2SJ022056−063934	0.330	18.35	Megacam/g	1.47 ± 0.04	1.25 ± 0.06	0.73 ± 0.04	76.6 ± 2.1	0.57 ± 0.01	105.0 ± 0.5	25.74 ± 0.09
SL2SJ022511−045433	0.238	16.84	WFPC2/F606W	1.90 ± 0.09	1.77 ± 0.09	0.58 ± 0.03	26.3 ± 0.2	0.75 ± 0.01	26.0 ± 0.7	24.14 ± 0.04
SL2SJ022610−042011	0.494	18.78	WFPC2/F606W	0.56 ± 0.03	1.15 ± 0.06	0.92 ± 0.06	5.3 ± 10.9	0.83 ± 0.01	56.2 ± 1.2	25.10 ± 0.08
SL2SJ022648−040610	0.766	20.01	WFPC2/F606W	1.20 ± 0.06	1.31 ± 0.07	0.82 ± 0.05	112.1 ± 5.2	0.34 ± 0.01	131.8 ± 0.6	26.17 ± 0.09
SL2SJ022648−090421	0.456	18.32	Megacam/g	1.30 ± 0.04	1.58 ± 0.09	0.83 ± 0.05	68.1 ± 4.2	0.81 ± 0.01	61.6 ± 0.9	27.13 ± 0.14
SL2SJ023251−040823	0.352	18.58	WFPC2/F606W	0.81 ± 0.04	1.10 ± 0.06	0.80 ± 0.04	122.0 ± 0.8	0.68 ± 0.01	110.2 ± 0.8	26.39 ± 0.08
SL2SJ140123+555705	0.526	19.14	WFPC2/F606W	0.76 ± 0.04	1.19 ± 0.07	0.49 ± 0.04	126.7 ± 6.5	0.73 ± 0.01	136.0 ± 1.1	25.19 ± 0.17
SL2SJ140614+520252	0.480	18.29	Megacam/g	2.15 ± 0.16	3.02 ± 0.15	0.29 ± 0.01	107.2 ± 0.1	0.48 ± 0.01	120.4 ± 0.6	23.50 ± 0.03
SL2SJ141137+565119	0.322	18.49	WFC3/F475X	0.76 ± 0.04	0.92 ± 0.05	0.90 ± 0.05	61.4 ± 0.3	0.88 ± 0.01	17.7 ± 1.4	25.86 ± 0.04
SL2SJ220629+005728	0.704	20.59	Megacam/g	2.25 ± 0.24	1.34 ± 0.07	0.46 ± 0.02	143.3 ± 0.2	0.99 ± 0.02	108.8 ± 5.1	25.81 ± 0.08
SL2SJ221326−000946	0.338	20.00	WFPC2/F606W	0.41 ± 0.02	1.08 ± 0.05	0.19 ± 0.01	138.0 ± 0.5	0.28 ± 0.01	148.4 ± 0.6	25.14 ± 0.04
SL2SJ221407−180712	0.650	20.43	WFPC2/F606W	0.57 ± 0.03	0.41 ± 0.23	0.69 ± 0.14	62.3 ± 46.9	0.73 ± 0.01	57.5 ± 0.8	25.29 ± 0.32
SL2SJ221606−175131	0.860	20.68	Megacam/g	0.93 ± 0.08	–	–	–	0.87 ± 0.01	57.4 ± 3.1	25.67 ± 0.07
SL2SJ221929−001743	0.289	17.78	Megacam/g	1.00 ± 0.03	0.74 ± 0.14	0.75 ± 0.15	85.3 ± 35.5	0.74 ± 0.01	84.3 ± 0.6	24.08 ± 0.21

Note. — Effective radii and associated errors are estimated from the mean and standard deviation of a `galfit` de Vaucouleurs fit in each of the r, i, and z Megacam bands when HST imaging is not available. When one or more HST bands are available, R_eff is measured on the reddest one (See table 1) but the error is still obtained from the Megacam bands. (a) As discussed in Section 4.1, we could not model SL2SJ221606−175131 as a lens and therefore do not report lensing parameters for this system.